

Article

Enhancement of Perovskite Photodetector Using MAPbI₃ with Formamidinium Bromide

Dong Jae Shin  and Hyung Wook Choi * 

Department of Electrical Engineering, Gachon University, Seongnam 13120, Republic of Korea; djshinyoon@gachon.ac.kr

* Correspondence: chw@gachon.ac.kr

Abstract: In this study, a perovskite-based mixed cation/anion ultraviolet photodetector with an added halide material is fabricated using perovskite combined with an ABX₃ structure. Mixed cation/anion perovskite thin films of MAPbI₃/FABr are manufactured through a relatively simple solution process and employed as light-absorption layers. In the produced thin film, SnO₂–sodium dodecylbenzenesulfonate acts as an electron transport layer and spiro-OMeTAD acts as a hole injection layer. Compared to a single cation/anion perovskite, the fabricated device exhibits phase stability and optoelectronic properties, and demonstrates a responsivity of 72.2 mA/W and a detectability of 4.67×10^{13} Jones. In addition, the films show an external quantum efficiency of 56%. This suggests that mixed cation/anion films can replace single cation/anion perovskite films. Thus, photodetectors based on lead halides that can be applied in various fields have recently been manufactured.

Keywords: deep-ultraviolet (UV) photodetectors; MAPbI₃; FABr

1. Introduction

In recent years, ultraviolet (UV) photodetectors have received considerable attention from researchers owing to their use in various fields such as covert communication, photo detecting, environmental analysis, astronomy, and medicine [1–3]. Generally, UV rays are divided into three areas according to wavelength range: UVA (~400–320 nm), UVB (~320–280 nm), and UVC (~280–100 nm) [1]. Most UVC rays are absorbed by the ozone layer and atmosphere and have no effect on Earth [4]. However, some UVC rays are radiated from technical light sources, like UV germicidal bulbs and mercury lamps [5]. UVC is harmful to human cells and can cause erythema and blindness [6,7]. Therefore, research on photodetectors that can detect UVC regions by converting incident optical signals into electrical signals is required.

Several types of inorganic materials such as Ga₂O₃, GaN, ZnGa₂O₄, and MoS₂/Si have been used for UV detection. However, processes that use inorganic semiconductor materials require sophisticated processing at high temperatures [8–10]. By contrast, the application of low-temperature solution processing using perovskite materials is increasing compared to that of other semiconductors [11–14].

At present, perovskites are considered as good materials for fabricating photodetectors owing to their ease of manufacturing and low operating voltage [15]. Additionally, hybrid organic–inorganic perovskites demonstrate advantages such as a large optical absorption coefficient, high carrier mobility, controlled band gap, and long diffusion length; consequently, the reported photodetectors based on halide perovskites can function in wide detection regions with a fast response speed [16].

Early research on optical devices using perovskites used methylammonium lead iodide (CH₃NH₃PbI₃, MAPbI₃), which was prepared using only MA⁺ monovalent A cations as the light absorber. However, problems such as photostability and thermal stability occur because of the low crystallization energy and phase transition between the tetragonal and cubic phases at ~320 K [17–19]. Therefore, the focus of research has shifted



Citation: Shin, D.J.; Choi, H.W.

Enhancement of Perovskite Photodetector Using MAPbI₃ with Formamidinium Bromide. *Energies* 2024, 17, 2183. <https://doi.org/10.3390/en17092183>

Academic Editor: Francesco Calise

Received: 28 March 2024

Revised: 22 April 2024

Accepted: 29 April 2024

Published: 2 May 2024



Copyright: © 2024 by the authors. Licensee MDPI, Basel, Switzerland. This article is an open access article distributed under the terms and conditions of the Creative Commons Attribution (CC BY) license (<https://creativecommons.org/licenses/by/4.0/>).

to engineering optimal perovskite configurations [20]. In this regard, formamidinium lead iodide ($\text{CH}(\text{NH}_2)_2\text{PbI}_3$, FAPbI₃) has been studied, owing to its higher decomposition temperature, longer diffusion length, excellent thermal stability, and narrow bandgap compared with MAPbI₃ [21]. However, FAPbI₃ has a trigonal structure (perovskite phase, black, and α -phase-FAPbI₃) or a hexagonal structure (non-perovskite phase, yellow, and δ -phase-FAPbI₃) depending on the synthesis temperature [22]. Because α -phase-FAPbI₃ is stable at high temperatures (above 160 °C), it can change into the more stable δ -phase-FAPbI₃ at room temperature [20]. This phase change degrades the performance of optical devices that use the fabricated perovskite film as a light-absorption layer. Therefore, to prevent this phase change and improve the performance of optical devices, research is being conducted to improve stability using a mixture of monovalent cations such as MA⁺, FA⁺, and CS⁺, or by adding halides such as Cl[−] and Br[−] [23,24].

In this study, mixed cation/anion perovskite films of MAPbI₃/FABr were produced as light-absorption layers to enhance the performance of perovskite deep-UV photodetectors. A more stable perovskite photodetector can be produced by adding a halide material (Br[−]) to the anti-solvent. When Br[−] ions are added, the Pb–Br bond length is relatively short, which reduces the lattice constant and improves the photogeneration and carrier transport characteristics. Additionally, because the ionic radius of the Br atom is smaller than that of I and the electronegativity of Br (2.96) is higher than that of I (2.66), the electronic charge distribution around the Br atom is much stronger, which can address the phase transition problem. Moreover, by adding Br ions, the bonding density of the perovskite can be increased, which can improve the efficiency of the film. Consequently, the prepared perovskite-based photodetector showed a photocurrent generation of 108.3 μA and a reactivity of 72.2 mA/W when FABr 20 was added to MAPbI₃. In addition, the photodetector exhibited a detection degree of 4.67×10^{13} Jones.

2. Materials and Methods

2.1. Reagents and Materials

All the materials and reagents were used without additional purification. Indium tin oxide (ITO) was coated on a quartz glass substrate (TMA, Seoul, Republic of Korea). A SnO₂ colloidal solution (15 wt% in water; Alfa Aesar, Haveril, MA, USA) was prepared. Furthermore, Pb(II) iodide (PbI₂; 99.999%), 1-butyl alcohol (99%), sodium dodecylbenzenesulfonate (SDBS), acetonitrile (99.93%), ethyl alcohol ($\geq 99.5\%$), dimethyl sulfoxide (DMSO; $\geq 99.9\%$), *N,N*-dimethylformamide (DMF; 99.8%), 2,2,7,7-tetrakis[*N,N*-di(4-methoxyphenyl)amino]-9,9-spirobifluorene (spiro-OMeTAD; 99%), 2-propanol (IPA; 75 wt%), bis(trifluoromethane)sulfonimide lithium salt (Li-TSFI; $\geq 99.0\%$), toluene (99.9%), and 4-*tert*-butylpyridine (98%) were all purchased from Sigma Aldrich, St. Louis, MO, USA. In addition, methylammonium iodide (MAI) and formamidinium bromide (FABr) were obtained from GreatCell SolarKorea, Seohyun, Republic of Korea.

2.2. Fabrication of MAPbI₃-Based Perovskite Photodetector

The ITO-deposited quartz substrates (8 Wm/sq) were purified to remove organic matter. Then, the substrates were sequentially cleaned using an ultrasonic bath with a neutral detergent, IPA, acetone, and purified water for 15 min each. Subsequently, the films were dried with UV ozone to remove any foreign substances. After diluting 1.2 mL of the SnO₂ colloidal solution with 5.2 mL of deionized water, 1 mg of SDBS was dissolved in the SnO₂ solution to make a SnO₂–SDBS mixed solution. To form the electron transport layer of the film, the SnO₂–SDBS mixed solution was spin-coated on an ITO substrate at 3000 rpm for 30 s and annealed at 150 °C for 30 min. The films were dried with UV ozone for 20 min to completely remove any moisture prior to the deposition of perovskite. The MAPbI₃ perovskite precursor solution was prepared by mixing PbI₂ (1.4 mol) and MAI (1.4 mol) in a mixture of DMF and DMSO (10:1, *v/v*). Next, IPA was stirred with FABr (0, 5, 10, 15, 20, and 25 mg) for 1 h to prepare the solution for FABr post-processing. The MAPbI₃ perovskite layer was spin-coated onto the SnO₂–SDBS layer at 4000 rpm for 25 s.

Subsequently, 250 μL of toluene was added dropwise 15 s before the end of the spin-coating to form an anti-solvent. The prepared post-processing solution was then spin-coated onto the MAPbI_3 layer at 4000 rpm for 25 s. The perovskite films were then annealed at 140 $^\circ\text{C}$ for 15 min on a hot plate. After cooling to room temperature, a spiro-OMeTAD solution [1 mL chlorobenzene containing 72.3 mg spiro-OMeTAD, 28.8 μL 4-tert-butyl pyridine, and 17.5 μL Li-TFSI solution (ACN in 1 mL of 520 mg Li-TFSI)] was coated onto the perovskite layer at 2000 rpm for 35 s. Finally, Au was thermally evaporated through an electrode using an e-beam evaporator in a high vacuum (2×10^{-6} Torr). Figure 1a shows the vertical structure of the fabricated photodetector and Figure 1b shows the preparation method.

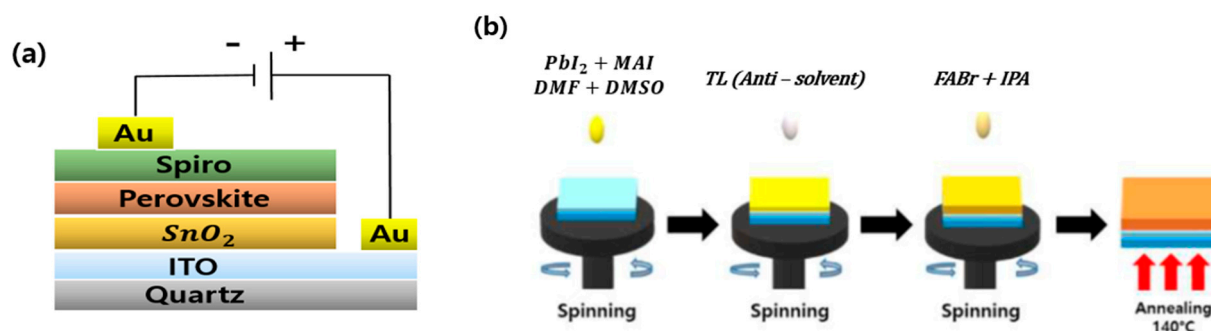


Figure 1. (a) Schematic diagram and (b) manufacturing process of MAPbI_3 -based deep-UV PD.

2.3. Device Characterization

To investigate the crystal structure of the fabricated film, XRD (SmartLab, Rigaku, Tokyo, Japan) analysis was performed using $\text{Cu K}\alpha$ radiation ($\lambda = 1.542 \text{ \AA}$). Field-emission SEM (Hitachi, S-4700, Tokyo, Japan) was used to analyze the surface and cross-sectional morphologies of the perovskite layers. The light absorptivity of the device was measured by UV-vis spectroscopy (UV-vis 8453, Agilent, Santa Clara, CA, USA). A combined source and measurement meter (Source Measure Unit, Keithley, 2400, Cleveland, OH, USA) was used to measure the electrical response of the perovskite photodetector. A UV lamp (6 W, 254 nm) (VL-6. LC, Vilber, VL6.LC, Seine-et-Marne, France) was used to provide 254 nm irradiation.

3. Results

Characteristics of the Prepared Perovskite Film

The perovskite films fabricated in this process are denoted as FABr 0, 5, 10, 15, 20, and 25, according to the amount of FABr added. Figure 2 shows the X-ray diffraction (XRD) patterns as a function of the amount of FABr added. The patterns indicate the crystal formation of the thin film after post-treatment with FABr. Figure 2a shows that the crystallinity of the films gradually enhanced as the FABr content increased. The reduced peak intensity in FABr 25 indicated that the high density of FABr caused grain shrinkage, which has a negative effect on film crystallization. The highest crystallinity was observed for FABr 20, and the intensity of the XRD peak was approximately 2.43 times that of the film without FABr. The growth of crystal grains owing to the addition of FABr leads to an increase in the extinction coefficient, which indicates the improved performance of the photodetector [25]. Figure 2b exhibits that with the addition of FABr, the main peak of MAPbI_3 shifts from 14.2° to 14.0° , which matches the main peak of FAPbI_3 . This peak shift suggests the formation of an $\text{FA}_x\text{MA}_{1-x}\text{PbI}_3$ perovskite thin film [26,27]. The lattice constant calculated by Bragg's law is 3.14 \AA at a diffraction angle of 14.2° , and increases to 3.184 \AA at 14.0° , which suggests that adding br-ions to the produced film increases mobility, allowing better current flow. It can be seen that the crystal size calculated using the Debye–Scherrer equation increases from 36.37 nm for FABr 0 to 39.98 nm for FABr 20. As a result, the produced $\text{FA}_x\text{MA}_{1-x}\text{PbI}_3$ film has high crystallinity. First, MAI and PbI_2 were dissolved in DMSO and DMF and filtered using a syringe filter. Subsequently, the prepared precursor solution was spin-coated on the ITO substrate on which SnO_2 was

deposited. In the intermediate step, the film was concentrated by solvent evaporation, and the spatial steric hindrance of FABr and DMSO prevented the conversion of layered PbI_2 into tetragonal perovskite. Subsequently, perovskite nucleation was accelerated through an anti-solvent process to crystallize the perovskite film with rapid solvent extraction. Finally, FABr was converted into the $\text{FA}_x\text{MA}_{1-x}\text{PbI}_3$ -DMSO phase via ion exchange. A highly crystalline perovskite film was formed through annealing [28].

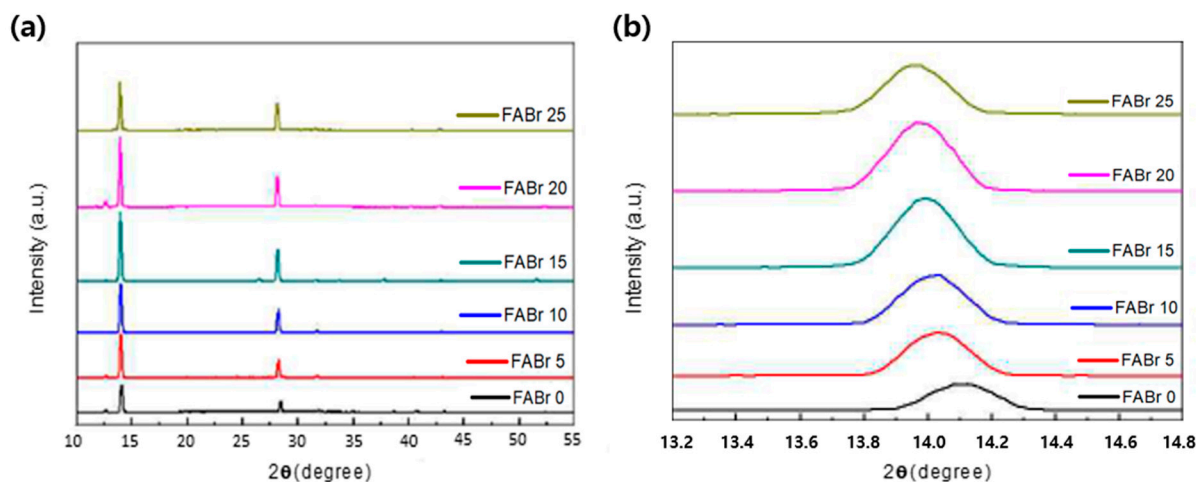


Figure 2. XRD patterns of $\text{FA}_x\text{MA}_{1-x}\text{PbI}_3$ films with different amounts of FABr added. (a) XRD patterns for different composition ratio and (b) expanded XRD patterns of the peaks from 13.0° to 15.0° .

Figure 3 shows the degree of surface formation of each fabricated perovskite film as observed using scanning electron microscopy (SEM). Figure 3a shows an SEM image of pure MAPbI_3 . It can be observed that the surface of FABr 0 has an irregular thin film. In addition, the particle sizes are relatively small. With the addition of the postprocessing solution, the size of the particles on the thin films also increased. In addition, the surface formation of the film improved, and a change in particle formation occurred. This implies improved photoelectric properties such as longer carrier life and better absorbance [29,30]. Figure 3e shows the most stable grain growth and uniform surface formation for FABr 20. However, Figure 3f shows that the grain size decreased and the number of pinholes increased in FABr 25. In addition, residues of PbI_2 are observed. This can be attributed to the de-wetting phenomenon caused by the addition of excessive FA cations [31]. Excessive FABr content may affect the quality of the film by microcrystallizing the remaining fine pattern material. Thus, the crystal grains become smaller and gaps appear throughout the thin film, which ultimately has a negative effect on the performance of the perovskite films. Therefore, the addition of more FABr than is necessary prevents the proper formation of the perovskite and causes a decrease in the performance. Consequently, changes in the grain size and surface shape depending on the concentration of added FABr suggest that the added FABr has a significant impact on the microstructural changes in the perovskite [32].

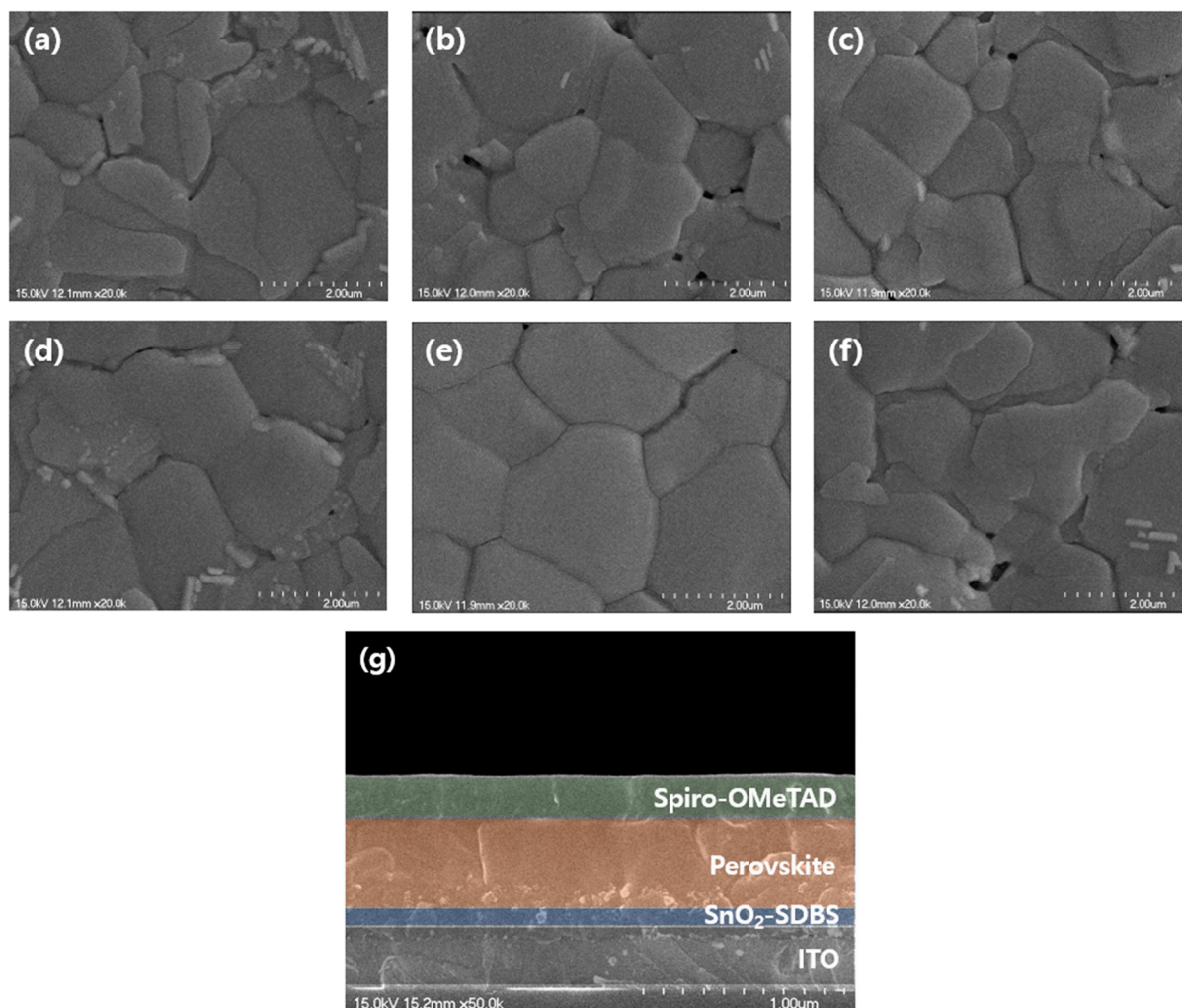


Figure 3. SEM images of $\text{FA}_x\text{MA}_{1-x}\text{PbI}_3$ films: (a) FAPbBr 0, (b) FAPbBr 5, (c) FAPbBr 10, (d) FAPbBr 15, (e) FAPbBr 20, and (f) FAPbBr 25. (g) Cross-section of a device with individual layers shown in different colors.

The UV-visible absorption spectra in Figure 4a show the absorbance of the fabricated film. With an increase in the amount of FAPbBr solution during the post-treatment process, the absorption spectrum showed a relative improvement. The films post-processed with FAPbBr exhibited better optical properties than that of FAPbBr 0. Furthermore, FAPbBr 20 exhibited the highest absorbance, and the decrease in the absorbance of FAPbBr-25 was affected by grain shrinkage owing to the excessive addition of FAPbBr. In addition, adding an optimal amount of Br improved the binding density of the particles, which is expected to improve the characteristics of the film, as shown in the absorbance measurement results [33].

Optoelectronic properties such as the resistivity, mobility, and carrier concentration of perovskite films are important characteristics of photodetector materials [34]. The photoelectric properties of the films with different concentrations of FAPbBr were analyzed through a Hall measurement system, and the results are shown in Figure 4b. The resistivity in FAPbBr 0 is $0.7704 \Omega\cdot\text{cm}$, and the perovskite films with added FAPbBr show resistivities of 0.2519 , 0.2975 , 0.2249 , 0.2077 , and $0.8474 \Omega\cdot\text{cm}$. The pure film (FAPbBr 0) exhibits a mobility of $5.01 \text{ cm}^2/\text{V}\cdot\text{s}$, whereas FAPbBr 20 exhibits a mobility of $25.48 \text{ cm}^2/\text{V}\cdot\text{s}$, which is the highest value obtained among the samples tested. The mobility is correlated with the Pb–Br structure. As the Pb–Br bond is relatively short, the lattice constant and distance between the atoms are reduced. Additionally, the electronegativity of the Br atom (2.96) is higher than that of I (2.66); therefore, heavy Pb hardly interacted with Br [35]. The decrease in

the mobility of FABr 25 can be attributed to the excessive amount of FABr added. The higher the mobility, the greater the photocurrent generated [36]. The parameter values of Resistivity, Mobility, and Carrier Concentration are shown in Table 1.

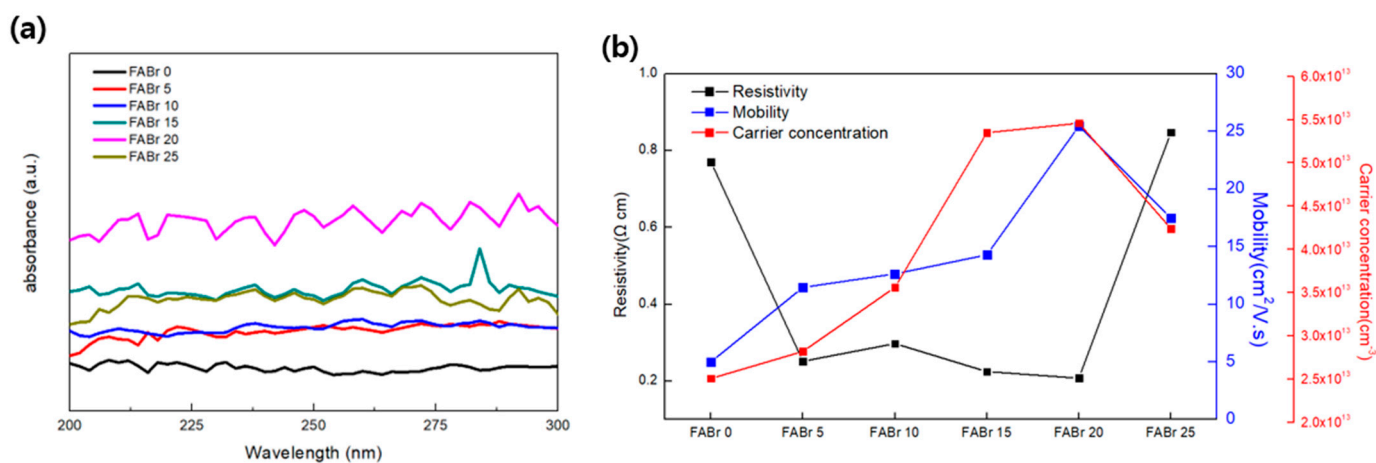


Figure 4. Characteristics of perovskite films: (a) UV-vis absorption spectra and (b) photoelectric characteristics.

Table 1. Parameters of resistivity, mobility, and carrier concentration for all films.

Sample	Resistivity (Ω·cm)	Mobility (cm ² /V·s)	Carrier Concentration (cm ⁻³)
FABr 0	0.7704	5.01	2.506×10^{13}
FABr 5	0.2519	11.47	2.821×10^{13}
FABr 10	0.2975	12.64	3.564×10^{13}
FABr 15	0.2249	14.29	5.358×10^{13}
FABr 20	0.2077	25.48	5.469×10^{13}
FABr 25	0.8474	17.48	4.242×10^{13}

The performance of the PD with respect to the amount of FABr added can be investigated by irradiating a 254 nm light with an output of 0.774 mW/cm² in dark conditions and analyzing the current–voltage (I–V) correlation from –2 to +2 V. Figure 5 shows the amount of photocurrent generated as a function of the amount of FABr added. The generation of a photocurrent is affected by the intensity and bias voltage of the irradiated light. At a voltage of 2 V, the amounts of generated photocurrents were 31.8, 51.6, 70.1, 85.2, 108.3, and 75.3 μA, respectively. The smallest amount of photocurrent was generated in FABr 0, and as the amount of added FABr increased, the amount of generated photocurrent also increased; consequently, the largest amount of photocurrent was generated in FABr 20. This is because the added FABr increased the particle size and crystal grains, thereby increasing the extinction coefficient, as shown in the SEM image and absorbance results.

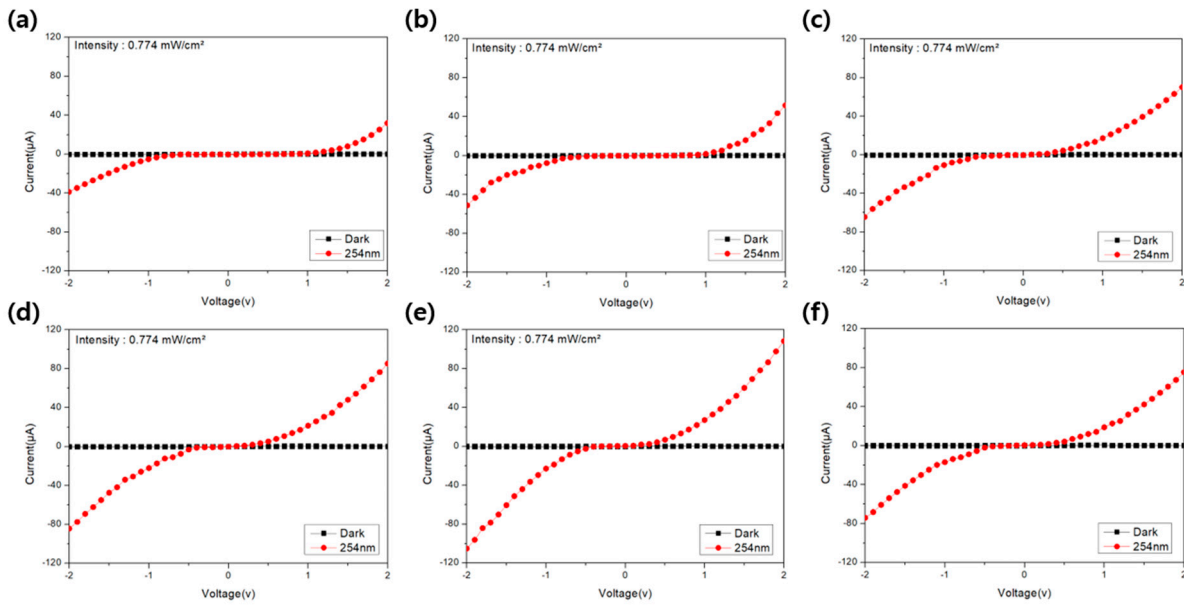


Figure 5. I–V curves of the UVC detector in a dark environment under 254 nm irradiation: (a) FABr 0, (b) FABr 5, (c) FABr 10, (d) FABr 15, (e) FABr 20, and (f) FABr 25.

Figure 6a shows the responsivity (R) and detectability (D^*) values of each thin film; R indicates the responsivity efficiency of the fabricated photodetector to the irradiated light. R is defined as the output photocurrent divided by the incident light power in the active area of the photodetector. It is determined by $R = (I_{\text{light}} - I_{\text{dark}}) / AP_{\text{op}}$ (I_{light} is the output current under 254 nm UV light, I_{dark} is the dark current, A is the active area of the PD, and P_{op} is the incident light power intensity). As the amount of FABr increased, the R values increased to 21.1, 34.4, 46.7, 56.8, and 72.2 mA/W. However, for FABr 25, the R value decreased to 50.2 mA/W. Furthermore, D^* is an important performance parameter indicating whether a PD region can be detected; D^* is related to the R value and the noise of the device, and can be confirmed through these characteristics. It is defined as $D^* = (A\Delta f)^{1/2} \Delta R / i_n$ (A is the effective area of the PD, Δf is the electrical bandwidth, and i_n is the current noise). Generally, it is calculated as $D^* = R / 2qJ_{\text{dark}}$. In this equation, q is the amount of charge and J_{dark} is the dark current density. R and D^* are proportional; as R increases, D^* also increases. The D^* value of the fabricated film increased to 1.74×10^{12} , 4.98×10^{12} , 2.38×10^{13} , 2.89×10^{13} , and 4.67×10^{13} Jones. However, in FABr 25, it decreased to 2.44×10^{13} Jones.

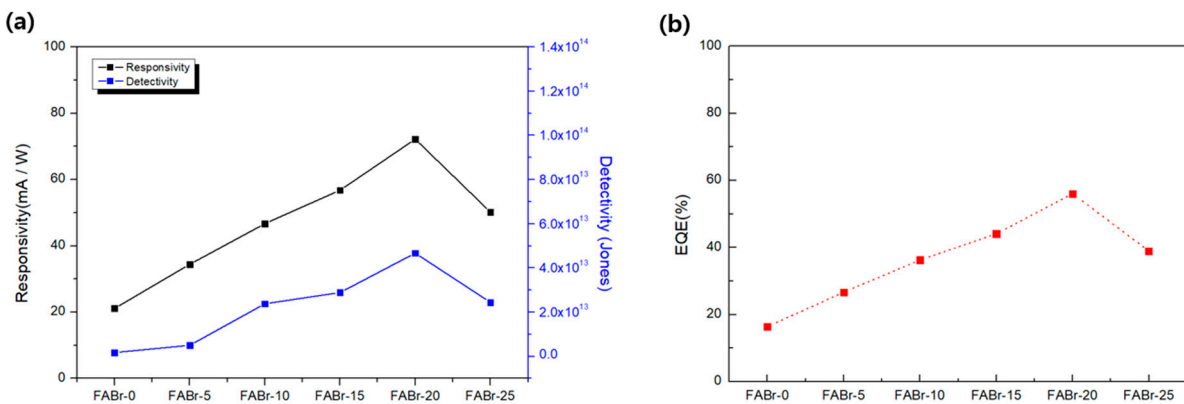


Figure 6. (a) Calculated R as a function of voltage and D^* ; (b) EQE.

Figure 6b shows the external quantum efficiency (EQE) of the photodetector as a function of the amount of added FABr. The EQE is defined as the ratio of the number of photons emitted to the number of electrons injected, and shows the conversion degree of

the PD; a high EQE indicates an excellent conversion efficiency of the photodetector. With an increase in the amount of added FABr, the EQE value at 2 V increased to 16, 27, 36, 44, and 56%; however, the EQE value decreased to 39% for FABr-25. This indicates that the mixed cation/anion perovskite film has better optoelectric properties than the single film. The R , D^* , and EQE values of the produced films are shown in Table 2.

Table 2. Performance parameters of PD according to the amount of FABr added.

Sample	Responsivity (mA/W)	Detectivity (Jones)	EQE (%)
FABr 0	21.1	1.74×10^{12}	16
FABr 5	34.4	4.98×10^{12}	27
FABr 10	46.7	2.38×10^{13}	36
FABr 15	56.8	2.89×10^{13}	44
FABr 20	72.2	4.67×10^{13}	56
FABr 25	50.2	2.44×10^{13}	39

Figure 7a shows the time-dependent optical response of the photodetector observed at a bias voltage of 1 V and an output light intensity of 0.774 mW/cm^2 . When the physical value input to the photodetector changes over time, the output of the UV PD cannot fluctuate immediately and there is a delay depending on the response time. Response speed refers to how quickly a sensor's output can fluctuate in response to input. This is one of the main parameters indicating the performance of the photodetector. The rise and fall times of the photodetector were measured to be 148 ms/164 ms, 164 s/171 ms, 224 ms/227 ms, 228 ms/231 ms, 227 ms/276 ms, and 228 ms/265 ms by increasing the amount of FABr added. This change occurs when numerous traps in the active layer briefly capture photocarriers before they are emitted, contributing to the circuit current and extending the fall time. Figure 7b shows the optical stability of the photodetector. Light stability can be checked by repeating ON/OFF 200 times at 3 s intervals. The optical current of $2.12 \text{ }\mu\text{A}$ in the first iteration was $2.18 \text{ }\mu\text{A}$ after 200 iterations. This section shows the improved stability of the photodetector.

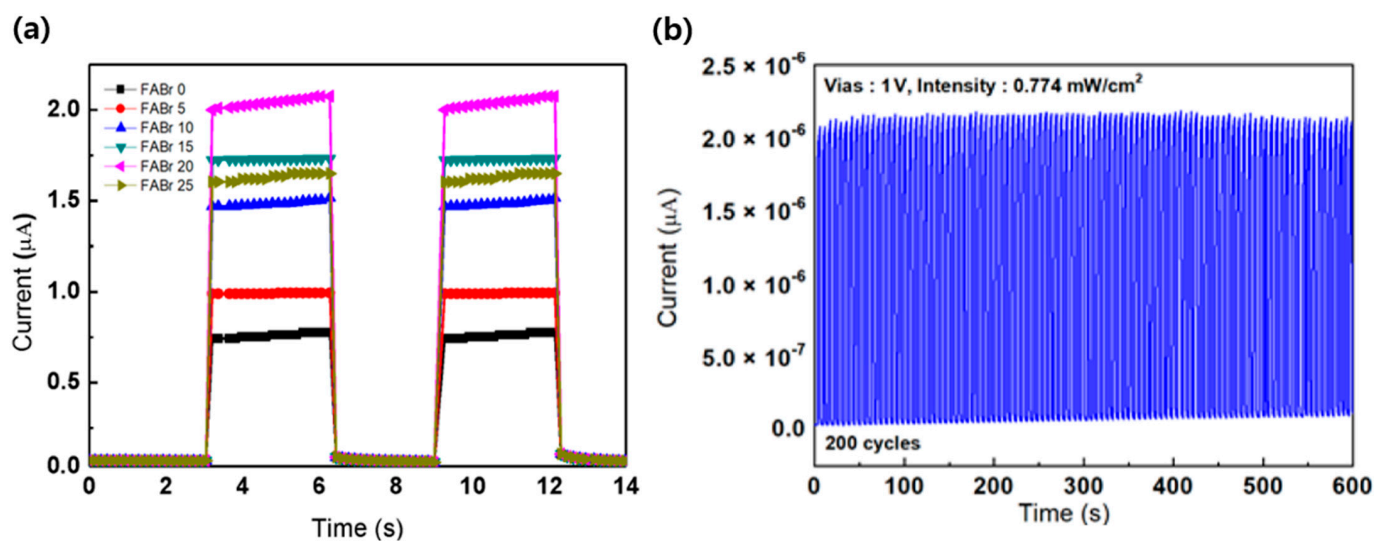


Figure 7. (a) Current-time characteristics of the photodetector according to the amount of FABr added; (b) photostability.

4. Discussion and Conclusions

In summary, a mixed cation/anion perovskite UVC photodetector is manufactured by adding FAPbBr to MAPbI₃ perovskite. When a halide material (Br⁻) was added to the anti-solvent, a more stable perovskite photodetector was obtained. The fabricated thin film showed better photoelectric properties under a 254 nm deep-UV light source, and FAPbBr 20 in particular showed the best photoelectric properties. This suggests that an optimal PD operation can be realized with the addition of an appropriate amount of FAPbBr. Therefore, these findings are expected to be useful in various fields.

Author Contributions: Sample fabrication and original draft preparation: D.J.S.; Supervision and editing: H.W.C. All authors have read and agreed to the published version of the manuscript.

Funding: The Authors have received research support from the Ministry of Education and Gachon University Research Grant.

Data Availability Statement: Data is unavailable due to privacy.

Acknowledgments: This research was supported by the Basic Science Research Capacity Enhancement Project through the Korea Basic Science Institute (National Research Facilities and Equipment Center) grant funded by the Ministry of Education (2019R1A6C1010016), and by the 2023 Gachon University Research Grant (GCU-202300810001).

Conflicts of Interest: The authors declare no conflict of interest.

References

1. Shi, L.; Nihtianov, S. Comparative study of silicon-based ultraviolet photodetectors. *IEEE Sens. J.* **2012**, *12*, 2453–2459. [[CrossRef](#)]
2. Yao, J.; Yang, G. 2D material broadband photodetectors. *Nanoscale* **2020**, *12*, 454–476. [[CrossRef](#)] [[PubMed](#)]
3. Nguyen, T.M.H.; Shin, S.G.; Choi, H.W.; Bark, C.W. Recent advances in self-powered and flexible UVC photodetectors. *Exploration* **2022**, *2*, 20210078. [[CrossRef](#)] [[PubMed](#)]
4. Zou, Y.; Zhang, Y.; Hu, Y.; Gu, H. Ultraviolet Detectors Based on Wide Bandgap Semiconductor Nanowire: A Review. *Sensors* **2018**, *18*, 2072. [[CrossRef](#)] [[PubMed](#)]
5. Gomes, C.C.; Preto, S. *Intelligent Human Systems Integration, IHSI 2018; Advances in Intelligent Systems and Computing*; Karwowski, W., Ahram, T., Eds.; Springer: Cham, Switzerland, 2018; Volume 722.
6. Narayanan, D.L.; Saladi, R.N.; Fox, J.L. Ultraviolet radiation and skin cancer. *Int. J. Dermatol.* **2010**, *49*, 978–986. [[CrossRef](#)] [[PubMed](#)]
7. Dixon, A.J.; Dixon, B.F. Ultraviolet radiation from welding and possible risk of skin and ocular malignancy. *Med. J. Aust.* **2004**, *181*, 155–157. [[CrossRef](#)] [[PubMed](#)]
8. Han, S.; Jin, W.; Zhang, D.; Tang, T.; Li, C.; Liu, X.; Liu, Z.; Lei, B.; Zhou, C. Photoconduction studies on GaN nanowire transistors under UV and polarized UV illumination. *Chem. Phys. Lett.* **2004**, *389*, 176–180. [[CrossRef](#)]
9. Tsai, S.H.; Basu, S.; Huang, C.Y.; Hsu, L.C.; Lin, Y.G.; Horng, R.H. Deep-ultraviolet photodetectors based on epitaxial ZnGa₂O₄ thin films. *Sci. Rep.* **2018**, *8*, 14056. [[CrossRef](#)] [[PubMed](#)]
10. Mendoza, F.; Makarov, V.; Weiner, B.R.; Morell, G. Solar-blind field-emission diamond ultraviolet detector. *Appl. Phys. Lett.* **2015**, *107*, 201605. [[CrossRef](#)]
11. Muscarella, L.A.; Petrova, D.; Cervasio, R.J.; Farawar, A.; Lugier, O.; McLure, C.; Slaman, M.J.; Wang, J.; Ehrler, B.; Hauff, E.V.; et al. Air-stable and oriented mixed lead halide perovskite (FA/MA) by the one-step deposition method using zinc iodide and an alkylammonium additive. *ACS Appl. Mater. Interfaces* **2019**, *11*, 17555–17562. [[CrossRef](#)]
12. Cruz, S.H.T.; Saliba, M.; Mayer, M.T.; Santiesteban, H.J.; Mathew, X.; Nienhaus, L.; Tress, W.; Erodici, M.P.; Sher, M.J.; Bawendi, M.G.; et al. Enhanced charge carrier mobility and lifetime suppress hysteresis and improve efficiency in planar perovskite solar cells. *Energy Environ. Sci.* **2018**, *11*, 78–86. [[CrossRef](#)]
13. Baena, J.P.C.; Steier, L.; Tress, W.; Saliba, M.; Neutzner, S.; Matsui, T.; Giordano, F.; Jacobsson, T.J.; Kandada, A.R.S.; Zakeeruddin, S.M.; et al. Highly efficient planar perovskite solar cells through band alignment engineering. *Energy Environ. Sci.* **2015**, *8*, 2928–2934. [[CrossRef](#)]
14. Wu, G.; Zhou, J.; Meng, R.; Xue, B.; Zhou, H.; Tang, Z.; Zhang, Y. Air-stable formamidinium/methylammonium mixed lead iodide perovskite integral microcrystals with low trap density and high photo-responsivity. *Phys. Chem. Chem. Phys.* **2019**, *21*, 3106–3113. [[CrossRef](#)] [[PubMed](#)]
15. Zhou, H.; Song, Z.; Tao, P.; Lei, H.; Gui, P.; Mei, J.; Wang, H.; Fang, G. Self-powered, ultraviolet-visible perovskite photodetector based on TiO₂ nanorods. *RSC Adv.* **2016**, *6*, 6205–6208. [[CrossRef](#)]
16. Wang, H.; Kim, D.H. Perovskite-based photodetectors: Materials and devices. *Chem. Soc. Rev.* **2017**, *46*, 5204–5236. [[CrossRef](#)]
17. Dualeh, A.; Gao, P.; Seok, S.I.; Nazeeruddin, M.K.; Gra, M. Thermal behavior of methylammonium lead-trihalide perovskite photovoltaic light harvesters. *Chem. Mater.* **2014**, *26*, 6160–6164. [[CrossRef](#)]

18. Lin, Q.; Armin, A.; Burn, P.L.; Meredith, P. Organohalide perovskites for solar energy conversion. *Acc. Chem. Res.* **2016**, *49*, 545–553. [[CrossRef](#)]
19. Wu, B.; Nguyen, H.T.; Ku, Z.; Han, G.; Giovanni, D.; Mathews, N.; Fan, H.J.; Sum, T.C. Discerning the surface and bulk recombination kinetics of organic–inorganic halide perovskite single crystals. *Adv. Energy Mater.* **2016**, *6*, 1600551. [[CrossRef](#)]
20. Jeon, N.J.; Noh, J.H.; Yang, W.S.; Kim, Y.C.; Ryu, S.; Seo, J.; Seok, S.I. Compositional engineering of perovskite materials for high-performance solar cells. *Nature* **2015**, *517*, 476–480. [[CrossRef](#)]
21. Aguiar, J.A.; Wozny, S.; Holesinger, T.G.; Aoki, T.; Patel, M.K.; Yang, M.; Berry, J.J.; Al-Jassim, M.; Zhou, W.; Zhu, K. In situ investigation of the formation and metastability of formamidinium lead tri-iodide perovskite solar cells. *Energy Environ. Sci.* **2016**, *9*, 2372–2382. [[CrossRef](#)]
22. Koh, T.M.; Fu, K.; Fang, Y.; Chen, S.; Sum, T.C.; Mathews, N.; Mhaisalkar, S.G.; Boix, P.P.; Baikie, T. Formamidinium-containing metal-halide: An alternative material for near-IR absorption perovskite solar cells. *J. Phys. Chem. C* **2014**, *118*, 16458–16462. [[CrossRef](#)]
23. Liu, J.; Shirai, Y.; Yang, X.; Yue, Y.; Chen, W.; Wu, Y.; Han, L. High-Quality Mixed-Organic-Cation Perovskites from a Phase-Pure Non-stoichiometric Intermediate (FAI)_{1-x}PbI₂ for Solar Cells. *Adv. Mater.* **2015**, *27*, 4918–4923. [[CrossRef](#)] [[PubMed](#)]
24. Saliba, M.; Matsui, T.; Domanski, K.; Seo, J.Y.; Ummadisingu, A.; Zakeeruddin, S.M.; Correa-Baena, J.P.; Tress, W.R.; Abate, A.; Hagfeldt, A.; et al. Incorporation of rubidium cations into perovskite solar cells improves photovoltaic performance. *Science* **2016**, *354*, 206–209. [[CrossRef](#)] [[PubMed](#)]
25. Slimi, B.; Mollar, M.; Assaker, I.B.; Kriaa, I.; Chtourou, R.; Mari, B. Perovskite FA_{1-x}MA_xPbI₃ for solar cells: Films formation and properties. *Energy Procedia* **2016**, *102*, 87–95. [[CrossRef](#)]
26. Guo, X.; Ngai, K.; Qin, M.; Lu, X.; Xu, J.; Long, M. The compatibility of methylammonium and formamidinium in mixed cation perovskite: The optoelectronic and stability properties. *Nanotechnology* **2020**, *32*, 075406. [[CrossRef](#)] [[PubMed](#)]
27. Li, X.; Yang, J.; Jiang, Q.; Chu, W.; Zhang, D.; Zhou, Z.; Ren, Y.; Xin, J. Enhanced photovoltaic performance and stability in mixed-cation perovskite solar cells via compositional modulation. *Electrochim. Acta* **2017**, *247*, 460–467. [[CrossRef](#)]
28. Yang, Y.; Peng, H.; Liu, C.; Arain, Z.; Ding, Y.; Ma, S.; Liu, X.; Hayat, T.; Alsaedi, A.; Dai, S. Bi-functional additive engineering for high-performance perovskite solar cells with reduced trap density. *J. Mater. Chem. A* **2019**, *7*, 6450–6458. [[CrossRef](#)]
29. Xu, X.; Ma, C.; Xie, Y.M.; Cheng, Y.; Tian, Y.; Li, M.; Tsang, S.W. Air-processed mixed-cation Cs_{0.15}FA_{0.85}PbI₃ planar perovskite solar cells derived from a PbI₂–CsI–FAI intermediate complex. *J. Mater. Chem. A* **2018**, *6*, 7731–7740. [[CrossRef](#)]
30. Bai, S.; Cheng, N.; Yu, Z.; Liu, P.; Wang, C.; Zhao, X.Z. Cubic: Column composite structure (NH₂CH=NH₂)_x(CH₃NH₃)_{1-x}PbI₃ for efficient hole-transport material-free and insulation layer free perovskite solar cells with high stability. *Electrochim. Acta* **2016**, *190*, 775–779. [[CrossRef](#)]
31. Jia, Y.H.; Neutzner, S.; Zhou, Y.; Yang, M.; Tapia, J.M.F.; Li, N.; Zhao, N. Role of Excess FAI in formation of high-efficiency FAPbI₃-based light-emitting diodes. *Adv. Funct. Mater.* **2020**, *30*, 1906875. [[CrossRef](#)]
32. Yang, Z.; Chueh, C.C.; Liang, P.W.; Crump, M.; Lin, F.; Zhu, Z.; Jen, A.K.Y. Effects of formamidinium and bromide ion substitution in methylammonium lead triiodide toward high-performance perovskite solar cells. *Nano Energy* **2016**, *22*, 328–337. [[CrossRef](#)]
33. Ni, X.; Lei, L.; Yu, Y.; Xie, J.; Li, M.; Yang, S.; Wang, M.; Liu, J.; Zhang, H.; Ye, B. Effect of Br content on phase stability and performance of H₂N=CHNH₂Pb(I_{1-x}Br_x)₃ perovskite thin films. *Nanotechnology* **2019**, *30*, 165402. [[CrossRef](#)] [[PubMed](#)]
34. Koizumi, S.; Umezawa, H.; Pernot, J.; Suzuki, M.M. *Power Electronics Device Applications of Diamond Semiconductors*; Woodhead Publishing: Sawston, UK, 2018; pp. 99–189.
35. Rehman, W.; Milot, R.L.; Eperon, G.E.; Wehrenfennig, C.; Boland, J.L.; Snaith, H.J.; Johnston, M.B.; Herz, L.M. Charge-carrier dynamics and mobilities in formamidinium lead mixed-halide perovskites. *Adv. Mater.* **2015**, *27*, 7938–7944. [[CrossRef](#)] [[PubMed](#)]
36. Myronov, M. Molecular Beam Epitaxy of High Mobility Silicon, Silicon Germanium and Germanium Quantum Well Heterostructures. In *Molecular Beam Epitaxy*; Elsevier: Amsterdam, The Netherlands, 2018; pp. 37–54.

Disclaimer/Publisher’s Note: The statements, opinions and data contained in all publications are solely those of the individual author(s) and contributor(s) and not of MDPI and/or the editor(s). MDPI and/or the editor(s) disclaim responsibility for any injury to people or property resulting from any ideas, methods, instructions or products referred to in the content.